Emodin ameliorates diabetic cardiomyopathy by regulating mitochondrial dynamics of fission and fusion and ferroptosis through the AHR-Nrf2 pathway

XINROU YU[1*], HAIFEI LOU[2*], JIEDONG ZHOU[3], HUI LIN[4,5], JINJING YANG[1] and JUFANG CHI[1]

[1]Department of Cardiology, Zhuji Affiliated Hospital of Wenzhou Medical University, Shaoxing, Zhejiang 311800, P.R. China; [2]Department of Emergency, The Affiliated Yangming Hospital of Ningbo University, Ningbo, Zhejiang 315040, P.R. China; [3]Department of Cardiovascular, The First Affiliated Hospital of Ningbo University, Ningbo University, Ningbo, Zhejiang 315010, P.R. China; [4]Department of Cardiovascular, The Affiliated Lihuili Hospital of Ningbo University, Healthy Science Center, Ningbo University, Ningbo, Zhejiang 315040, P.R. China; [5]Department of Cardiology, Shaoxing People's Hospital (Shaoxing Hospital, Zhejiang University School of Medicine), Shaoxing, Zhejiang 312000, P.R. China

Received February 5, 2026; Accepted October 23, 2026

DOI: 10.3892/ijmm.2026.6041

Abstract. Emodin, a natural anthraquinone with known antioxidant properties, has not been fully investigated in diabetic cardiomyopathy (DCM), a condition marked by oxidative stress, ferroptosis and metabolic disturbance, and lacking specific therapies. A DCM model was induced by streptozotocin and a high-fat diet. Cardiac function after emodin treatment was assessed via echocardiography, while myocardial injury, fibrosis and myocardial iron concentration were evaluated histologically. Mitochondrial fission-fusion dynamics were examined using transmission electron microscopy and confocal imaging. *In vitro* functional rescue experiments using Ferrostatin-1 and aryl hydrocarbon receptor (AHR) knockdown via small interfering RNA or AAV9 was performed to determine its role in emodin-regulated ferroptosis, lipid peroxidation, mitochondrial dynamics and Nrf2 signaling. Emodin improved left ventricular systolic function, attenuated metabolic disorders, reduced myocardial iron concentration and fibrosis, and suppressed excessive mitochondrial fission and lipid peroxidation in DCM mice. These effects were largely reversed by AHR knockdown. Mechanistically, emodin promoted Nrf2 nuclear translocation and upregulated antioxidant molecules, while AHR silencing abrogated these protective effects, thereby exacerbating ferroptosis and mitochondrial dynamic imbalance. In conclusion, emodin protects against high glucose-induced cardiac injury and improves mitochondrial function by limiting ferroptosis and restoring mitochondrial fission-fusion homeostasis, effects that are mediated through the AHR-Nrf2 pathway. These findings suggest emodin and the AHR-Nrf2 axis as potential therapeutic targets for DCM.

Correspondence to: Dr Jinjing Yang or Ms. Jufang Chi, Department of Cardiology, Zhuji Affiliated Hospital of Wenzhou Medical University, 9 Jianmin Road, Taozhu, Zhuji, Shaoxing, Zhejiang 311800, P.R. China
E-mail: 779154572@qq.com
E-mail: jf_chi@163.com

*Contributed equally

Key words: diabetic cardiomyopathy, emodin, aryl hydrocarbon receptor, Nrf2, mitochondria

Introduction

Poor blood sugar control can lead to numerous complications of diabetes, with diabetic cardiomyopathy (DCM) being one of the common causes of death associated with diabetes. DCM is a prevalent cardiovascular disease with a heavy medical burden, expected to affect 783.2 million people by 2045, with healthcare costs reaching 1.054 trillion USD (1). Systemic metabolic disorders, inflammation, and oxidative stress are key pathophysiological factors in DCM. These factors lead to ferroptosis and apoptosis, resulting in impaired myocardial contraction and relaxation, left ventricular hypertrophy, and ultimately heart failure (2). Among these pathological factors, oxidative stress plays a crucial role. Current treatments for DCM primarily focus on controlling the underlying disease, and there is a lack of specific cardioprotective drugs (3). Therefore, it is particularly important to investigate the mechanisms of DCM and find appropriate drugs to modulate redox balance, apoptosis, and ferroptosis.

Heart is an energy-intensive organ that requires substantial energy for contraction. As a result, cardiomyocytes typically contain a large number of mitochondria. However, in environments with high blood glucose and insulin resistance, the microenvironment of cardiomyocytes is disrupted, leading to damage of the mitochondrial respiratory chain. This accelerates the imbalance of mitochondrial fission and fusion, resulting in prolonged production of reactive oxygen species (ROS) and subsequent oxidative stress (4,5). Oxidative stress and mitochondrial dysfunction are mutually reinforcing; sustained

ROS production causes mitochondrial damage, disruption of protein post-translational modifications, inflammation, myocardial fibrosis and hypertrophy, ultimately leading to cardiomyocyte apoptosis and heart failure (6). Additionally, the generation of ROS and mitochondrial damage are key mechanisms of ferroptosis. Ferroptosis is characterized by the accumulation of iron and ROS, and glutathione peroxidase 4 (GPX4) is a marker of ferroptosis (7), playing a crucial role in antioxidant defense. Ferroptosis has been confirmed to be associated with various diseases (8,9). Therefore, inhibiting ferroptosis may be a new target for DCM.

Emodin (PubChem CID: 3220; 1,3,8-Trihydroxy-6-methylanthraquinone, emo) is an anthraquinone compound found in various traditional Chinese medicines, including aloe, cassia seeds and rhubarb. Researchers have discovered that anthraquinone compounds not only possess antitumor, anti-inflammatory, immunosuppressive and analgesic effects, but also are a new type of ferroptosis inhibitor (10-12). Increasing evidence shows that emo has also made significant breakthroughs in the field of cardiovascular diseases. Previous research by the authors indicates that emo inhibits doxorubicin-induced heart failure by modulating the gut microbiota (13). Additionally, emo can improve LPS-induced myocardial injury by inhibiting NLRP3 inflammasome activation (14). In hypoxia models, emo protects against hypoxia-induced damage by upregulating miR-138 (15). He *et al* (12) found that aloin can activate the Nrf2 pathway to increase downstream antioxidant genes, thereby alleviating DOX-induced oxidative stress injury and inhibiting ferroptosis in cardiomyocytes. However, research on emo in DCM is very limited. Currently, only a previous study has confirmed that emo prevents the progression of DCM by upregulating the AKT/GSK-3β signaling pathway (16). There is a lack of research on emo's regulation of high glucose-induced ferroptosis and mitochondrial dysfunction.

The aryl hydrocarbon receptor (AHR) is a ligand-dependent transcription factor. In the absence of a ligand, AHR resides in the cytoplasm. Upon ligand binding, AHR translocates to the nucleus, where it interacts with AHR nuclear translocator to regulate the expression of target genes (17,18). AHR has been shown to be closely related to various physiological processes such as immune regulation, intestinal barrier function and tumor microenvironment. Crucially, literature evidence has established that AHR can directly function as an upstream transcription factor for Nrf2, thereby activating its transcription and driving antioxidant defense (19). Nrf2 is a transcription factor with antioxidant properties, playing a crucial role in numerous disease models by exerting antioxidant effects. In diabetic retinopathy, the Keap1-Nrf2 pathway provides significant antioxidant protection (20). In the nervous system, activating Nrf2 and inhibiting the NF-kB pathway can improve Alzheimer's disease (21). Previous research by the authors indicates that emo can reshape the gut microbiota structure disrupted by DOX, and the beneficial metabolites produced activate Nrf2 to exert cardioprotective effects. Whether emo can also protect the heart in DCM by activating the AHR-Nrf2 pathway is a question worth investigating (13).

In the present study, it was hypothesized that emo can alleviate ferroptosis and mitochondrial fission-fusion dynamics disturbances in cardiomyocytes, thereby protecting the heart under high glucose stress, and that these effects are mediated by the AHR-Nrf2 pathway.

Materials and methods

Animal experiments. All animal procedures followed the 'Guidelines for Animal Care and Use' and received approval from the Shaoxing People's Hospital Ethics Committee for Experimental Research (approval no. 2022C020; Shaoxing, China). In total, 24 male C57BL/6J mice (5 weeks old, weight from 18 to 25 g) were purchased from Zhejiang Chinese Medical University. Before the experiment began, the mice were housed for one week at 25±2˚C with free access to standard rodent chow and water. After the acclimation period, the mice were randomly divided into four groups: Control group, DCM group, DCM + low dose group, and DCM + high dose group. Throughout the experiment, mice in the control group received a standard diet, while all other groups were fed a high-sugar, high-fat and high-cholesterol diet. After 8 weeks, all groups except for the control group received continuous intraperitoneal injection of streptozotocin (STZ, 55 mg/kg body weight, 0.1 mol/l citric acid carrier, pH 4.5) for 3 days. Mice with random blood glucose levels reaching 11.1 mmol/l or higher for three consecutive days were considered to have successfully induced diabetes (22,23). Following successful induction of diabetes, and while continuing on the high-fat diet (HFD), mice in the DCM + low dose group were gavaged daily with 10 mg/kg/day of emo (MedChemExpress), and mice in the DCM + high dose group were gavaged daily with 30 mg/kg/day of Emo, last for 16 weeks.

Cardiac ultrasound imaging. A total of 1 week before the end of the experiment, cardiac ultrasound imaging was performed. Mice were anesthetized with isoflurane (3% for induction and 1-2% for maintenance), and left ventricular end-systolic diameter, left ventricular end-diastolic diameter, left ventricular ejection fraction (LVEF) and left ventricular fractional shortening (LVFS) were measured using the VisualSonics Vevo 2100 Imaging System.

Sample collection. For each mouse, nasal hair was removed, and 1 ml of peripheral blood was collected from the retro-orbital venous sinus under isoflurane anesthesia (5% for induction, delivered at an oxygen flow rate of 2 l/min). The mice were then euthanized by cervical dislocation. Subsequently, the skull and cervical vertebrae were rapidly dissected. The carcasses were immersed in 75% ethanol, and the sternum was opened to quickly collect the hearts. The hearts were rinsed in pre-cooled PBS, flash-frozen in liquid nitrogen, and stored at -80˚C until analysis.

Histopathological examination. Hearts were perfused with physiological saline to remove red blood cells and then immediately fixed in 10% formalin at 4˚C for 48 h. After the tissue underwent gradient dehydration, it was embedded in a paraffin machine to prepare 5-μm paraffin sections. Hematoxylin and eosin staining was performed using a staining kit (Beyotime Institute of Biotechnology) to assess myocardial morphology. Masson's trichrome stain (Wuhan Servicebio Technology Co.,

Ltd.) was be applied to observe fibrotic myocardial interstitium. The cross-sectional area of cardiomyocytes was observed by staining cell membranes with FITC-labeled WGA (Wuhan Servicebio Technology Co., Ltd.). Images of the stained slides were captured using a Leica DM3000 microscope (Leica Microsystems GmbH), and image quantification was performed using Image-ProPlus 6 (Media Cybernetics, Inc.).

Transmission electron microscopy (TEM) and Flameng Scoring. Apical heart fragments ~1 mm in length were sequentially double-fixed with 2.5% glutaraldehyde and 1% osmium tetroxide, dehydrated through a graded acetone series, infiltrated with propylene oxide and embedded in epoxy resin. After ultrathin sectioning, the grids were counter-stained with 2% uranyl acetate and 0.2% lead citrate. Mitochondrial images were finally acquired on a spherical-aberration-corrected transmission electron microscope (Titan G2 60-300). The degree of mitochondrial ultrastructural injury in myocardial tissues was blindly evaluated under TEM using the 0-4 scale Flameng grading system (0, normal mitochondrial structure with intact granules; 1, normal structure with granule loss; 2, swollen mitochondria with a clear matrix; 3, disrupted cristae and transparent matrix; 4, ruptured inner and outer membranes). Five fields were randomly selected per sample, and 20 mitochondria were evaluated per field to calculate the mean score for statistical analysis.

Blood glucose and biomarker detection. During the final week of the experiment, random blood glucose levels were measured for three consecutive days using a Yuwell blood glucose meter (Yuwell). For each measurement, ~5 μl of blood was collected from the tail vein. At the end of the experiment, terminal blood samples were collected from the retro-orbital venous sinus and centrifuged to obtain serum. The concentrations of glutathione (GSH), lactate dehydrogenase (LDH), malondialdehyde (MDA) and superoxide dismutase (SOD) in serum were detected using ELISA kits (GSH, cat. no. A006-2-1; LDH, cat. no. A020-2-2; MDA, cat. no. A003-1-2; SOD, cat. no. A001-2-2; all from Nanjing Jiancheng Bioengineering Institute). Serum triglyceride (TG) levels were determined using a tissue TG enzymatic assay kit (Applygen Technologies, Inc.). Myocardial iron content was measured using an Iron Assay Kit (Beyotime Institute of Biotechnology) according to the manufacturer's instructions.

Cell culture and treatment. H9C2 cells were obtained from the Cell Bank of the Chinese Academy of Sciences and cultured in Dulbecco's Modified Eagle's Medium (DMEM) containing 10% fetal bovine serum (Gibco; Thermo Fisher Scientific, Inc.) at 37˚C in a humidified atmosphere with 5% CO_2. Cells were cultured to 70-80% confluence before experiments. To establish a high-glucose (HG) toxicity model, cells were incubated in HG medium (33 mM) for 48 h. To validate the role of AHR *in vitro*, AHR-targeted small interfering RNA (si-AHR) (Obio Technology Corp., Ltd.) was used to interfere with AHR expression. The sequences of the small interfering RNAs used for RNA interference are detailed in Table SI.

Five groups were established: Control, HG, HG + emo, siNC + HG + emo, and siAHR + HG + emo. The Control group received no treatment, with a medium glucose concentration of 5.5 mM. The other groups underwent HG stimulation for 48 h as described. The HG + emo group was then treated with 40 μM Emo and incubated for 24 h. For the siNC + HG + emo and siAHR + HG + emo groups, 30 nM of siRNA was applied to 60% confluent cells using Lipofectamine 3000 (Invitrogen; Thermo Fisher Scientific, Inc.) in Opti-MEM medium (Gibco; Thermo Fisher Scientific, Inc.). Transfection was performed at 37˚C for 6 h, after which the transfection medium was replaced with fresh culture medium. After 48 h, HG stimulation and 40 μM emo incubation were conducted as aforementioned.

Ferrostatin-1 (Fer-1) treatment and cell viability assay. For ferroptosis inhibition experiments, H9C2 cells were pretreated with Fer-1 (cat. no. HY-100579; MedChemExpress) at different concentrations for 2 h prior to HG stimulation. Subsequently, cells were exposed to HG medium and treated with Emodin as aforementioned. Cell viability was assessed using a Cell Counting Kit-8 (CCK-8) assay (cat. no. HY-K0301; MedChemExpress). Briefly, H9C2 cells were seeded into 96-well plates at a density of 2,000 cells/well in 100 μl of culture medium and subjected to the indicated treatments. After treatment, 10 μl of CCK-8 reagent was added to each well and incubated at 37˚C for 2 h according to the manufacturer's instructions. The absorbance at 450 nm was measured using a microplate reader, and cell viability was expressed relative to the control group.

Immunofluorescence staining of Nrf2 in vivo and in vitro. H9C2 cells were fixed with 4% paraformaldehyde at room temperature for 15 min and permeabilized using 0.1% Triton. Following permeabilization, the cells were blocked with 10% BSA (cat. no. HY-D0842; MedChemExpress) at 37˚C for 30 min. They were then incubated with the Nrf2 antibody (1:200; cat. no. AF0639; Affinity Biosciences) overnight at 4˚C. Afterward, the cells were treated for 1 h with Alexa Fluor 594-conjugated goat anti-rabbit secondary antibody (1:200; cat. no. SA00013-4; Proteintech Group, Inc.). Finally, nuclear staining was performed with DAPI (0.005 mg/ml), and images were acquired using a confocal microscope (Leica Biosystems).

Detection of cellular ROS. Intracellular ROS levels were assessed using a ROS assay kit (cat. no. S0033S; Beyotime Institute of Biotechnology). Following the manufacturer's protocol, the cell culture medium was removed, and an appropriate volume of diluted DCFH-DA staining solution was added. Cells were incubated at 37˚C in a cell culture incubator for 20 min. After incubation, the cells were washed three times with serum-free medium to eliminate any excess fluorescent dye that had not penetrated the cells. Images were captured using a confocal microscope (Leica Biosystems).

Lipid peroxidation assay. Lipid peroxidation during ferroptosis was assessed using BODIPY lipid peroxidation fluorescent probes (Beyotime Institute of Biotechnology). According to the manufacturer's instructions, cells at the appropriate density were incubated with the probe in the dark for 1 h, washed twice with PBS, and observed under a confocal laser microscope at excitation wavelengths of 488 and 565 nm.

Mitochondrial morphology imaging and quantification. Mitochondria of viable H9C2 cells were specifically labeled using 200 nM Mito-Tracker Red (cat. no. C1035; Beyotime Institute of Biotechnology), and nuclei were stained with Hoechst (cat. no. C1018; Beyotime Institute of Biotechnology). Images of mitochondrial morphology were acquired using a laser confocal scanning microscope (Leica Biosystems). Morphometric analysis was performed in ImageJ software (version 1.54t; National Institutes of Health); the mitochondrial channel was background-subtracted, thresholded, and analyzed with Analyze Particles to derive mean mitochondrial size (fold of control) and number of mitochondria per cell. Six cells per group were analyzed by a blinded investigator.

In vivo transfection of adeno-associated virus. The cTnT promoter-driven AAV9 vector was constructed to package small hairpin RNA (shRNA) targeting AHR (AAV9-shAHR) or its negative control (AAV9-shNC), which were supplied by Hanbi Biotechnology Co., Ltd. In total, 24 5-week-old male C57BL/6J mice were purchased from Zhejiang Chinese Medical University. After one week of acclimation, all mice were fed HFD. A total of 1 week before model induction, each mouse was injected via the tail vein with AAV9-shNC or AAV9-shAHR at a dose of $2x10^{11}$ viral genomes (v.g.) per mouse, diluted in 150 μl of sterile normal saline. After successful model induction, emodin was administered by gavage at a dose of 30 mg/kg/day or an equal volume of normal saline was given for 16 weeks. The mice were divided into four groups: AAV9-NC + DCM group, AAV9-NC + DCM + emo group, AAV9-shAHR + DCM group, and AAV9-shAHR + DCM + emo group.

Western blotting. Total protein was extracted from heart tissues or H9C2 cells using RIPA lysis buffer (Beyotime Institute of Biotechnology) containing phosphatase inhibitor cocktail II (MedChemExpress). Protein concentrations were determined using an enhanced bicinchoninic acid (BCA) protein assay kit (cat. no. P0010; Beyotime Institute of Biotechnology) according to the manufacturer's instructions. Equal amounts of protein (20 μg per lane) were separated by SDS-PAGE using 10% polyacrylamide gels and transferred onto PVDF membranes. After blocking with 5% non-fat milk for 1 h at room temperature, the membranes were incubated overnight at 4˚C with specific primary antibodies, followed by incubation with HRP-conjugated secondary antibodies at room temperature for 1 h. Protein bands were visualized using enhanced chemiluminescence (Beyotime Institute of Biotechnology) and quantified with Image-Pro Plus 6 software (Media Cybernetics, Inc.). The specific primary antibodies used in this study included: Anti-dynamin-related protein 1 (DRP1; 1:2,000; cat. no. ab184247; Abcam), anti-mitochondrial fusion protein 1 (MFN1; 1:2,000; cat. no. ab126575; Abcam), anti-MFN2 (1:2,000; cat. no. ab124773; Abcam), anti-optic atrophy protein 1 (OPA1; 1:1,500; cat. no. ab119685; Abcam), anti-GPX4 (1:1,000; cat. no. DF6701; Affinity Biosciences), anti-acyl-CoA synthase long chain family member 4 (ACSL4; 1:1,000; cat. no. 38493; Cell Signaling Technology, Inc.), anti-solute carrier family 7 member 11 (SLC7A11; 1:1,000; cat. no. 98051; Cell Signaling Technology, Inc.), anti-AHR (1:1,000; cat. no. AF6278; Affinity Biosciences), anti-Nrf2 (1:2,000; cat. no. ab62352; Abcam), anti-heme oxygenase 1 (HO-1; 1:1,000; cat. no. AF5393; Affinity Biosciences), anti-quinone oxidoreductase 1 (NQO1; 1:1,000; cat. no. DF6437; Affinity Biosciences), TfR1 (1:1,000; cat. no. 10084-e2-AP; Proteintech Group, Inc.), FTH1 (1:1,000; cat. no. 11682-1-AP; Proteintech Group, Inc.) and anti-β-actin (1:1,000; cat. no. AF7018; Affinity Biosciences).

Assessment of mitochondrial membrane potential (MMP). The MMP was measured using a JC-1 assay kit (Beijing Solarbio Science & Technology Co., Ltd.). After the specified interventions, 2.5 mmol/l JC-1 dye was added to the H9C2 cells and incubated in the dark at 37˚C for 30 min. Images were captured using a laser confocal scanning microscope (Leica Biosystems). Red fluorescence indicates JC-1 aggregates representing normal, highly polarized membrane potential, while green fluorescence indicates JC-1 monomers representing the loss of MMP.

Reverse transcription-quantitative PCR (RT-qPCR). Total RNA from mouse myocardial tissues was extracted using the FastPure Complex Tissue/Cell Total RNA Isolation Kit (cat. no. RC113-01; Vazyme Biotech Co., Ltd.). Subsequently, RT-qPCR amplification was performed using the HiScript II One Step RT-qPCR SYBR Green Kit (cat. no. Q221-01; Vazyme Biotech Co., Ltd.) to detect the relative mRNA expression of AHR in myocardial tissues. The reaction conditions were set as follows: i) 95˚C for 10 min, ii) 40 cycles of 95˚C for 10 sec and 60˚C for 30 sec, iii) 72˚C for 15 sec. GAPDH was used to normalize the target genes via the $2^{-\Delta\Delta Cq}$ method (24). The primers used in the present study were shown in Table SII.

Molecular docking. Molecular docking was performed to investigate the potential interaction between emodin and AHR. The three-dimensional structure of emodin was obtained from PubChem (CID: 3220), and the AHR structure was retrieved from the Protein Data Bank (PDB ID: 5NJ8). The protein and ligand structures were prepared using PyMOL and AutoDockTools, respectively. Molecular docking was performed using AutoDock Vina (version 1.1.2; The Scripps Research Institute). The predicted binding pose and protein-ligand interactions were analyzed using PyMOL and the Protein-Ligand Interaction Profiler (PLIP).

Statistical analysis. All data were presented as the mean ± SD (standard deviation). Statistical analysis was performed using SPSS 22.0 (IBM Corp.), and graphs were generated using Prism 8 software (GraphPad; Dotmatics). A two-tailed unpaired Student's t-test was used for comparisons between two groups, and one-way or two-way ANOVA followed by Tukey's multiple comparisons test was used for comparisons among more than two groups. $P<0.05$ was considered to indicate a statistically significant difference.

Results

Emo improves cardiac ejection dysfunction induced by high glucose. To investigate the protective effect and dose-dependence of emo on DCM, emo was administered by gavage for 16 weeks to C57BL/6J mice induced by a high-sugar, high-fat

and high-cholesterol diet combined with STZ injection (Fig. 1A). Throughout the experimental period, the metabolic characteristics were evaluated. Compared with the control group, mice in the DCM group exhibited metabolic alterations, characterized by a decrease in body weight alongside increases in blood glucose and serum TG levels (Fig. S1A-C, $P<0.01$), indicating the induction of the diabetic phenotype. The cardiac functions of each group were further evaluated by echocardiography. Compared with the control group, the DCM mice showed significant cardiac function impairment, manifested as significantly reduced LVEF and LVFS ($P<0.01$). Meanwhile, echocardiography showed that LVIDd and LVIDs in the DCM group were significantly enlarged, suggesting marked ventricular dilation (Fig. 1B-F). By contrast, after 16 weeks of emo treatment, cardiac function was significantly improved in a dose-dependent manner. Low-dose treatment increased LVEF and LVFS to a certain extent, while high-dose treatment demonstrated a stronger protective effect. In addition, high-dose treatment significantly reversed ventricular remodeling, and LVIDd and LVIDs were significantly smaller than those in the DCM group ($P<0.01$) (Fig. 1B-F). The dose-dependent decrease in serum creatine kinase-MB levels (Fig. 1G) further confirmed that emo treatment could alleviate diabetic myocardial injury.

Cardiac hypertrophy and interstitial fibrosis are the characteristic pathological changes of DCM. As shown in Fig. 1H-M, compared with the control group, the hearts of the DCM group exhibited typical pathological changes. The increase in the ratio of heart weight to tibial length (Fig. 1H), the disordered and broken arrangement of central muscle fibers in H&E staining (Fig. 1I), the intensified interstitial fibrosis shown by MASSON staining (Fig. 1J and K), and the increase in the cross-sectional area of myocardial cells indicated by WGA staining (Fig. 1L and M) were verified. Emo treatment improved the above-mentioned cardiac pathological changes caused by diabetes, especially the high-dose treatment group effectively alleviated the myocardial damage caused by long-term diabetes. These findings suggested that emo significantly alleviated myocardial hypertrophy and interstitial fibrosis caused by diabetes in a dose-dependent manner, thereby improving cardiac remodeling in DCM.

Emo alleviates mitochondrial dynamic imbalance in DCM mice and reduces ferroptosis. To explore whether emo exerts a protective effect by regulating mitochondrial division and fusion. The mitochondrial structure was observed by electron microscopy (Fig. 2A). The results demonstrated that compared with the control group, the mice treated with DCM had mitochondrial abnormalities, including mitochondrial crest destruction, increased porosity, increased membrane density and membrane rupture, which was indicated by an increase in Flameng scores (Fig. S1F). In addition, the average size of individual mitochondria in mice treated with DCM decreased and the mitochondrial density per unit area increased compared with the control group (Fig. 2B and C). The enzymatic activity of the mitochondrial complex was additionally measured (Fig. 2D). The results showed that compared with the control group, the activities of mitochondrial complexes I and III in the DCM group were impaired, while complexes II and IV were basically unaffected. The aforementioned results suggest that the mitochondrial oxidative respiratory chain is damaged, the generation of superoxides increases, and tissue oxidative stress intensifies. However, the aforementioned results were reversed after emo intervention. Emo exerts a protective effect by regulating mitochondrial division and fusion. The aforementioned conjecture was verified by detecting the relevant proteins (Fig. 2E-I). Compared with the control group, the mitochondrial dynamics in the DCM group were severely imbalanced, among which the expression of the key protein DRP1 mediating mitochondrial division was significantly upregulated. Conversely, the expression levels of MFN1 and MFN2 for outer mitochondrial membrane fusion and OPA1 for inner membrane fusion were significantly downregulated. This change pattern indicates excessive mitochondrial division in DCM cardiomyocytes. Emo treatment effectively reversed this imbalance. The low-dose of emo slightly reversed the expression of the aforementioned proteins, and the high-dose of emo strongly inhibited the expression of DRP1 and increased the protein levels of MFN1, MFN2 and OPA1.

Mitochondrial dynamics imbalance can lead to the production of a large amount of ROS. The accumulated ROS can damage cellular proteins, lipids and DNA, cause lipid peroxidation, damage cells and tissues, and eventually lead to ferroptosis. As an iron-dependent form of cell death, ferroptosis is characterized by iron overload. Consistent with this, colorimetric absolute quantification revealed an iron accumulation in the myocardial tissues of DCM mice (Fig. S1D). Immunoblotting analysis revealed that the expression level of GPX4 in the DCM group was significantly lower than that in the control group. Moreover, the expression of SLC7A11, a key transporter for synthesizing glutathione, decreased significantly, while the expression of ACSL4, which promotes lipid peroxidation, was significantly upregulated (Fig. 2J-M). It is worth noting that emo treatment inhibited ferroptosis in DCM mice, reversed the aforementioned results, and counterbalanced the cardiac ferroptosis damage induced by high sugar and high fat, with the high-dose group having the strongest protective effect. The relevant serological indicators also verified the aforementioned results (Fig. 2N-Q). Compared with the control group, the serum LDH activity and MDA content in the DCM group were significantly increased, while the SOD activity and GSH level were significantly decreased. Emo treatment could dose-dependently reduce LDH and MDA, increase SOD and GSH, and the high-dose group had the strongest improvement effect. It is suggested that emo can alleviate ferroptosis in DCM and protect cardiomyocytes. The aforementioned results clearly show that there is a significant mitochondrial dynamic imbalance in DCM. Emo effectively inhibits ferroptosis in cardiomyocytes in DCM by reshaping mitochondrial dynamic balance (inhibiting division and promoting fusion) and improving mitochondrial function, thereby exerting a protective effect on the heart. To investigate the role of ferroptosis inhibition in the effects of emo and to evaluate the expression of iron metabolism-related proteins, *in vitro* treatment was subsequently conducted utilizing the specific ferroptosis inhibitor Ferrostatin-1 (Fer-1).

Emo regulates ferroptosis in DCM mice through the AHR-Nrf2 pathway. To reveal the specific mechanism by which emo regulates ferroptosis, focus was addressed on the

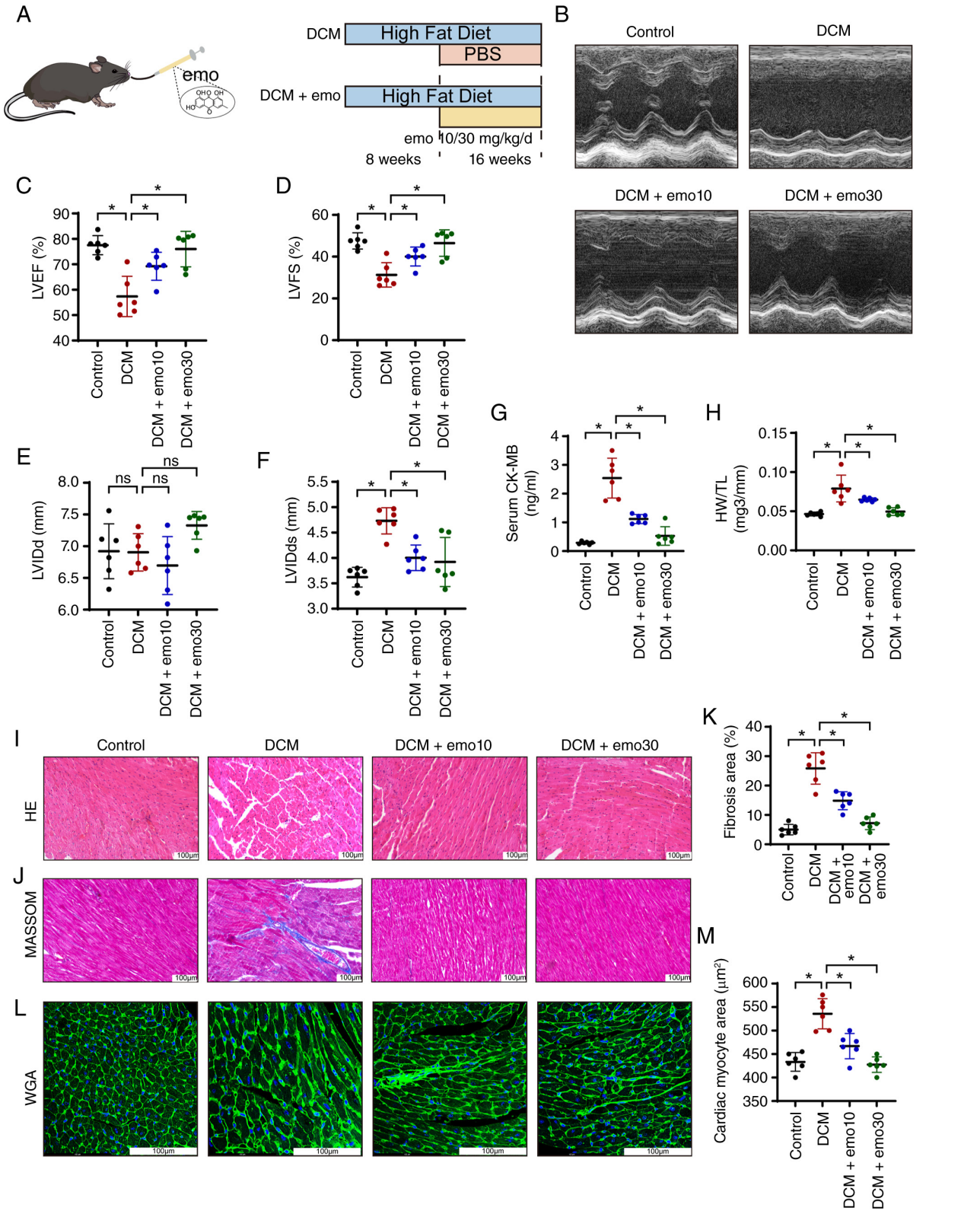


Figure 1. Emodin improves cardiac ejection function and reduces myocardial injury in DCM. (A) Schematic diagram of the animal experimental protocol. (B) M-mode echocardiography. (C-F) LVEF, LVFS, LVIDd and LVIDs measured by M-mode echocardiography. (G) Serum cardiac injury markers CK-MB measured by ELISA. (H) HW/TL ratio for each group of mice. (I) H&E staining to assess myocardial morphology. (J) Masson staining to detect myocardial fibrosis. (K) Quantification of fibrosis area in Masson staining. (L) WGA staining to evaluate myocardial hypertrophy. (M) Quantification of average myocardial cell area. Data are presented as the mean ± SD (n=6 per group). *P<0.05. DCM, diabetic cardiomyopathy; LVEF, left ventricular ejection fraction; LVFS, left ventricular fractional shortening; LVID, left ventricular internal dimension; LVIDd, LVID at end-diastole; LVIDs, LVID at systole; CK-MB, creatine kinase-MB; HW/TL, heart weight/tibial length; ns, not statistically significant.

key role of AHR in metabolic disorders. Molecular docking prediction indicates that emo can specifically bind to AHR (Fig. 3A). Consistently, RT-qPCR revealed that the relative mRNA expression of AHR in the myocardial tissues of the

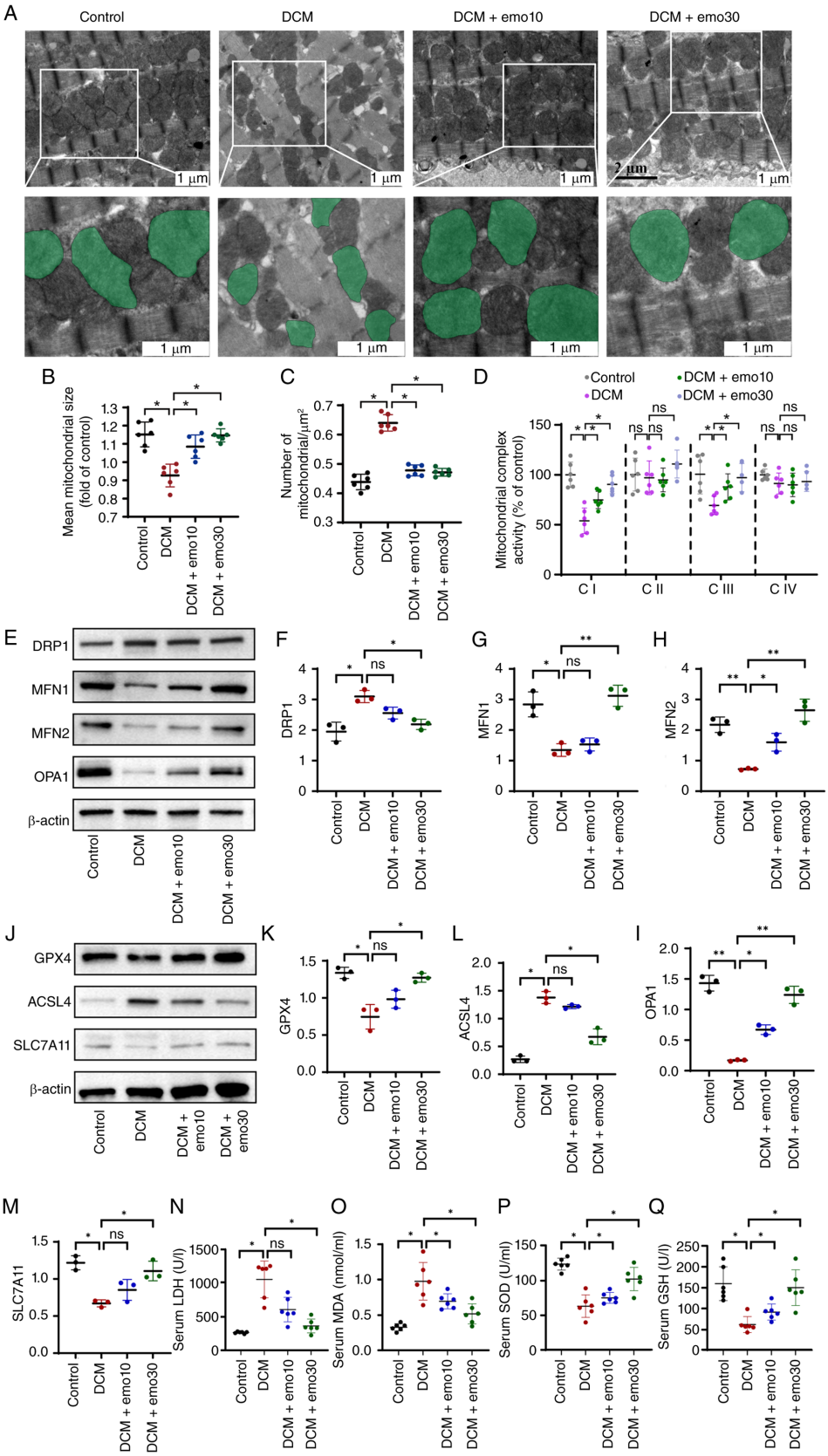


Figure 2. Emodin alleviates mitochondrial dynamic imbalance in the myocardium of DCM mice and reduced ferroptosis. (A) Representative mitochondrial images obtained by transmission electron microscopy, with the bottom images (magnified from the top images) showing representative mitochondria marked in light green pseudocolor to highlight mitochondrial changes. (B and C) Quantitative data on average mitochondrial size and the number of mitochondria per μm^2. (D) Quantitative assessment of mitochondrial respiratory chain complex activity. (E-I) Western blot analysis of the relative protein expression levels of DRP1, MFN1, MFN2 and OPA1 *in vivo*. (J-M) Western blot analysis of the relative protein expression levels of GPX4, ACSL4 and SLC7A11 *in vivo*. (N-Q) Serum redox markers LDH, MDA, SOD and GSH measured by ELISA. Data are presented as the mean ± SD (n=6 independent animal experiments; n=3 independent western blot experiments). *P<0.05 and **P<0.01. DCM, diabetic cardiomyopathy; DRP1, dynamin-related protein 1; MFN, mitochondrial fusion protein; OPA1, optic atrophy protein 1; GPX4, glutathione peroxidase 4; ACSL4, acyl-CoA synthase long chain family member 4; SLC7A11, solute carrier family 7 member 11; MDA, malondialdehyde; SOD, superoxide dismutase; GSH, glutathione; ns, not statistically significant.

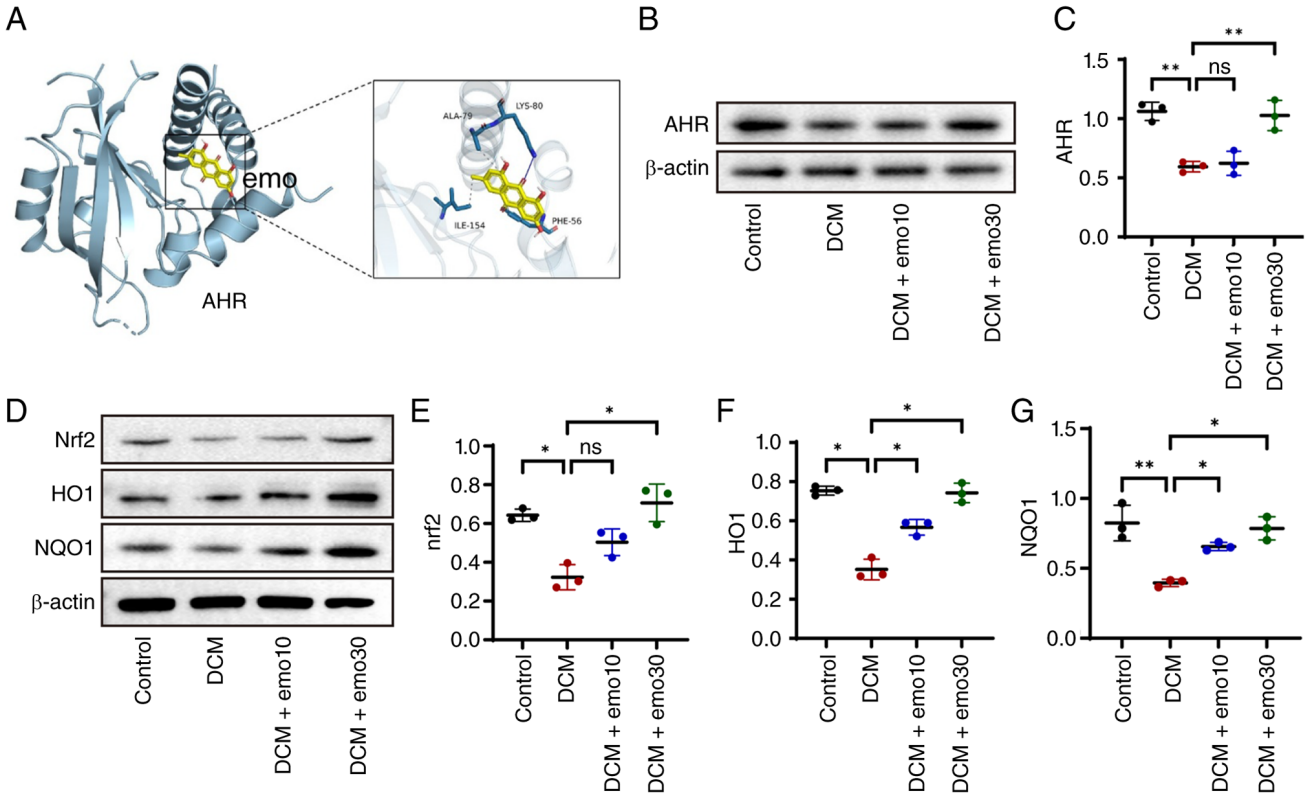


Figure 3. Emodin regulates ferroptosis metabolism in DCM mice through the AHR-Nrf2 pathway. (A) Cartoon model demonstrating the binding interaction and secondary structure of emo with AHR. (B and C) Western blot analysis of AHR protein expression in myocardial tissue. (D-G) Western blot analysis of expression levels of Nrf2 and downstream antioxidant molecules HO-1 and NQO1. Data are presented as the mean ± SD (n=3). *P<0.05 and **P<0.01. DCM, diabetic cardiomyopathy; AHR, aryl hydrocarbon receptor; HO-1, heme oxygenase 1; NQO1, quinone oxidoreductase 1; ns, not statistically significant.

DCM group was decreased compared with the control group, an effect that was dose-dependently increased by emo treatment (Fig. S1E). The expression of AHR was detected by western blotting, which was consistent with the predicted results of molecular docking (Fig. 3B and C). The expression of AHR in the DCM group was inhibited compared with that in the control group. After emo treatment, the expression of AHR increased in a dose-dependent manner. Given that the activation of AHR regulates Nrf2, the expression of Nrf2 was further examined (Fig. 3D and E). The results revealed that compared with the control group, the protein level of Nrf2 in the cell nucleus of the DCM group was significantly decreased. Correspondingly, the protein expression levels of its key downstream antioxidant enzymes, HO-1 and NQO1, were also significantly downregulated. This indicates that in the DCM state, the core antioxidant defense system within the cells is impaired in function. However, emo treatment effectively reversed this phenomenon. In the emo treatment group, it could be observed that the level of Nrf2 protein in the cell nucleus and the expression levels of HO-1 and NQO1 increased significantly (Fig. 3D-G). These results indicate that emo can dose-dependently activate the AHR-Nrf2 signaling pathway, thereby enhancing the endogenous antioxidant capacity of cardiomyocytes, inhibiting the production of ROS, and alleviating ferroptosis.

Emo alleviates high glucose-induced ferroptosis via an AHR dependent way. The cytoprotective mechanism of emo against HG-elicited ferroptosis in H9C2 cardiomyoblasts was investigated in the present study. In the absence of HG stress, emo up to 40 μM did not alter basal cell viability (Fig. 4A). CCK-8 assays revealed that emo dose-dependently attenuated HG-induced H9C2 injury, conferring significant cytoprotection (Fig. 4B). Based on these viability data, while 20 μM showed substantial protection, 40 μM emo elicited the maximum cytoprotective effect without causing basal cytotoxicity. Therefore, 40 μM was selected as the optimal effective concentration for subsequent mechanistic experiments. Western blot analysis demonstrated that HG significantly downregulated AHR protein expression relative to control, whereas concomitant emo treatment restored AHR levels above those observed in the HG group (P<0.05), indicating that emo reverses HG-mediated suppression of AHR (Fig. 4C and D).

To verify the crucial role of the AHR-mediated transcriptional network in emo protection, a specific AHR siRNA was used to knockdown its expression in H9C2 cells. Among them, AHR siRNA3 had the best knockdown effect and was selected for subsequent application (Fig. 5A and B). The localization of Nrf2 under different interventions was observed by fluorescence staining. Compared with the control, HG stimulation led to a weakened fluorescence intensity of Nrf2. However, after emo treatment, a significant increase in Nrf2 nuclear translocation could be clearly observed. Importantly, the emo-induced promotion of Nrf2 nuclear translocation was significantly abolished following the knockdown of AHR (Fig. 5C). The results of western blotting found that compared with the control group, the expression levels of Nrf2, NQO1 and HO-1 proteins in the HG group were significantly decreased. The aforementioned

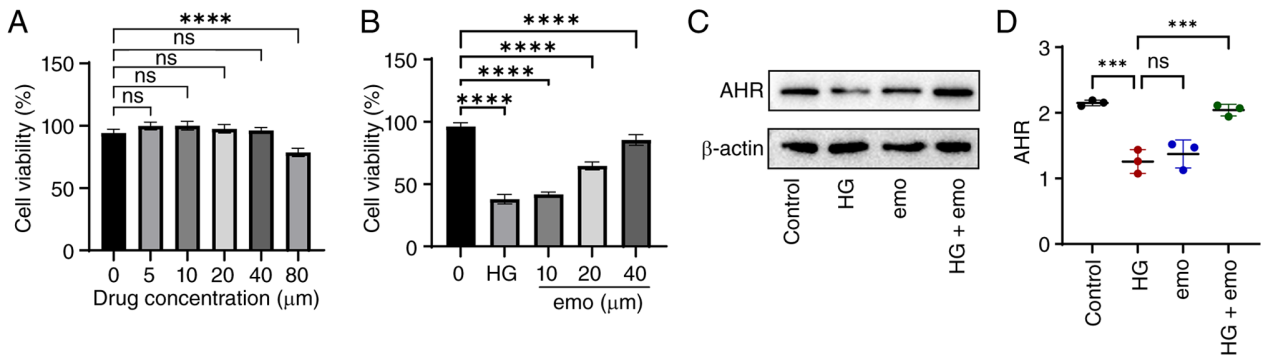


Figure 4. Determination of the Optimal Emo Dosing Concentration. (A and B) Cell Counting Kit-8 assays showing cell viability after 24 h treatment with varying concentrations of emo. (C and D) Western blot analysis of AHR in H9C2 cells in each group. Data are presented as the mean ± SD (n=3). ***P<0.001 and ****P<0.0001. AHR, aryl hydrocarbon receptor; HG, high-glucose; ns, not statistically significant.

results were reversed after treatment with emo. However, the emo-induced upregulation of Nrf2, NQO1 and HO-1 was significantly suppressed when AHR was silenced (compared with the HG + emo group, P<0.05, Fig. 5D-G). These findings demonstrate that emo promotes Nrf2 activation and its downstream antioxidant defense in an AHR-dependent manner.

Subsequently, the intracellular ROS levels were detected. Compared with the Control group, the ROS fluorescence intensity and IOD/Area value in the HG group were significantly increased. However, the ROS level was significantly reversed after emo intervention. Notably, the inhibitory effect of emo on ROS production was largely neutralized in the siAHR + HG + emo group (Fig. 5H and I). Similarly, BODIPY staining on H9C2 cells was used to detect the level of lipid ROS. The results demonstrated that compared with the HG group, the green fluorescence intensity of intracellular lipid peroxidation decreased after emo treatment, suggesting that emo alleviated lipid peroxidation in HG cardiomyocytes induced by high glucose. However, in AHR-deficient cardiomyocytes, the protective effect of emo against lipid peroxidation was markedly diminished (Fig. 5J and K). Western blotting revealed that the HG-induced downregulation of GPX4 and SLC7A11 and upregulation of ACSL4 were reversed by emo. Crucially, the anti-ferroptotic effect of emo was significantly attenuated after AHR knockdown (Fig. 5L-O). Collectively, these results indicate that emo exerts its antioxidant and anti-ferroptotic effects by activating the AHR-Nrf2 signaling axis.

To evaluate the potential involvement of ferroptosis in HG-induced cardiomyocyte injury, H9C2 cells were treated with different concentrations of Fer-1. As revealed in Fig. S2A, Fer-1 treatment increased the viability of HG-stimulated H9C2 cells. Therefore, 10 μM Fer-1 was used in subsequent experiments. Furthermore, BODIPY staining showed that both Emodin and Fer-1 reduced HG-induced lipid peroxidation (Fig. S2B and C). Subsequently, the protein expression of the iron-uptake marker TfR1, the iron-storage protein FTH1, the core anti-ferroptotic enzyme GPX4 and the pro-ferroptotic lipid metabolism enzyme ACSL4 were assessed (Fig. S2D-H). Consistent with previous observations, HG stimulation significantly upregulated the pro-ferroptotic drivers TfR1 and ACSL4 while suppressing the defense proteins FTH1 and GPX4 (P<0.05), indicating a pathological state of intracellular iron overload and unchecked lipid peroxidation. Notably, emo treatment effectively reversed these changes, mirroring the molecular profile of Fer-1 intervention. Specifically, both emo and Fer-1 restored GPX4 levels and normalized iron metabolism by downregulating TfR1 and upregulating FTH1. These findings provide compelling functional evidence that emo protects H9C2 cells against HG-induced injury by maintaining iron homeostasis and inhibiting the ferroptotic pathway.

Emo activates AHR to reshape the mitochondrial dynamic balance of cardiomyocytes induced by HG. Previous studies demonstrated that mitochondrial dynamics imbalance plays a key role in cell damage induced by HG (25). To verify that emo reshapes the mitochondrial dynamic balance of cardiomyocytes induced by HG through AHR mediation, the effect of AHR knockdown on mitochondrial dynamics was studied *in vitro*. Mitochondria were labeled using mitochondrial probes and images were captured under confocal microscopy. The results showed that HG caused marked mitochondrial fragmentation, whereas emo reversed this phenotype and restored elongated rod-like mitochondria; these effects were lost after AHR knockdown (Fig. 6A and B). The changes in MMP were evaluated using the JC-1 detection kit. The results revealed that emo also normalized HG-induced MMP loss, which was again abolished by AHR silencing (Fig. 6C and D). Consistently, emo decreased DRP1 and increased MFN1, MFN2 and OPA1 expression, shifting mitochondrial dynamics from fission toward fusion, while AHR inhibition reversed these changes (Fig. 6E-I). This indicates that in *in vitro* experiments, emo intervention to activate the AHR pathway effectively reshaped the mitochondrial dynamic balance of H9C2 cells induced by HG. Importantly, to investigate whether the mitochondrial dynamic alterations and ferroptosis are causally linked or merely parallel outcomes, mitochondrial morphology was evaluated following ferroptosis inhibition. Strikingly, the pharmacological inhibition of ferroptosis by Fer-1 decreased HG-induced mitochondrial fragmentation, maintaining the elongated rod-like mitochondrial networks (Fig. S2I-K). At the molecular level, western blot analysis revealed that Fer-1 treatment reversed the HG-induced molecular imbalance of mitochondrial dynamics, evidenced by the downregulation of the fission mediator DRP1 and the restoration of core fusion proteins, including MFN1, MFN2 and OPA1 (Fig. S2L-P). These critical findings unequivocally demonstrate that mitochondrial dynamic collapse is not an

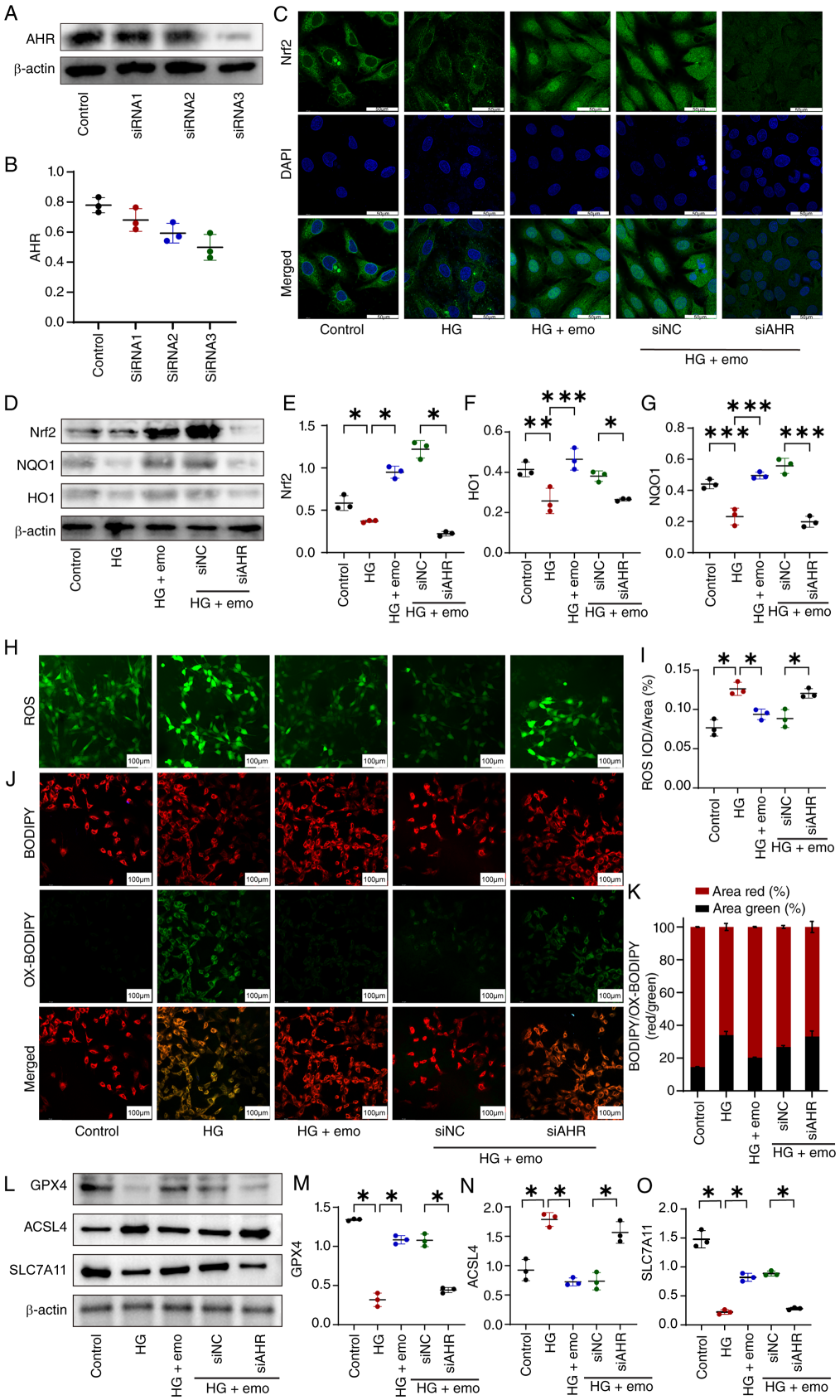


Figure 5. Emodin improves lipid peroxidation in cardiomyocytes induced by high glucose *in vitro* and alleviates ferroptosis, and this effect requires AHR mediation. (A and B) Western blot analysis to verify the efficiency of siRNA-mediated AHR knockdown. (C) Representative images showing Nrf2 distribution in cultured H9C2 cells. (D-G) Western blot analysis of Nrf2 and downstream antioxidant molecules NQO1 and HO-1 expression in H9C2 cells in each group. (H and I) DCFH-DA fluorescent probe observation of ROS production in H9C2 cells across different groups. (J and K) BODIPY staining to detect lipid peroxidation in H9C2 cells (red: reduced BODIPY; green: oxidized BODIPY). (L-O) Western blot analysis of the relative protein expression of GPX4, ACSL4 and SLC7A11 in H9C2 cells. Data are presented as the mean ± SD (n=3). *P<0.05, **P<0.01 and ***P<0.001. AHR, aryl hydrocarbon receptor; siRNA, small interfering RNA; NQO1, quinone oxidoreductase 1; HO-1, heme oxygenase 1; ROS, reactive oxygen species; NC, negative control; GPX4, glutathione peroxidase 4; ACSL4, acyl-CoA synthase long chain family member 4; SLC7A11, solute carrier family 7 member 11; HG, high-glucose.

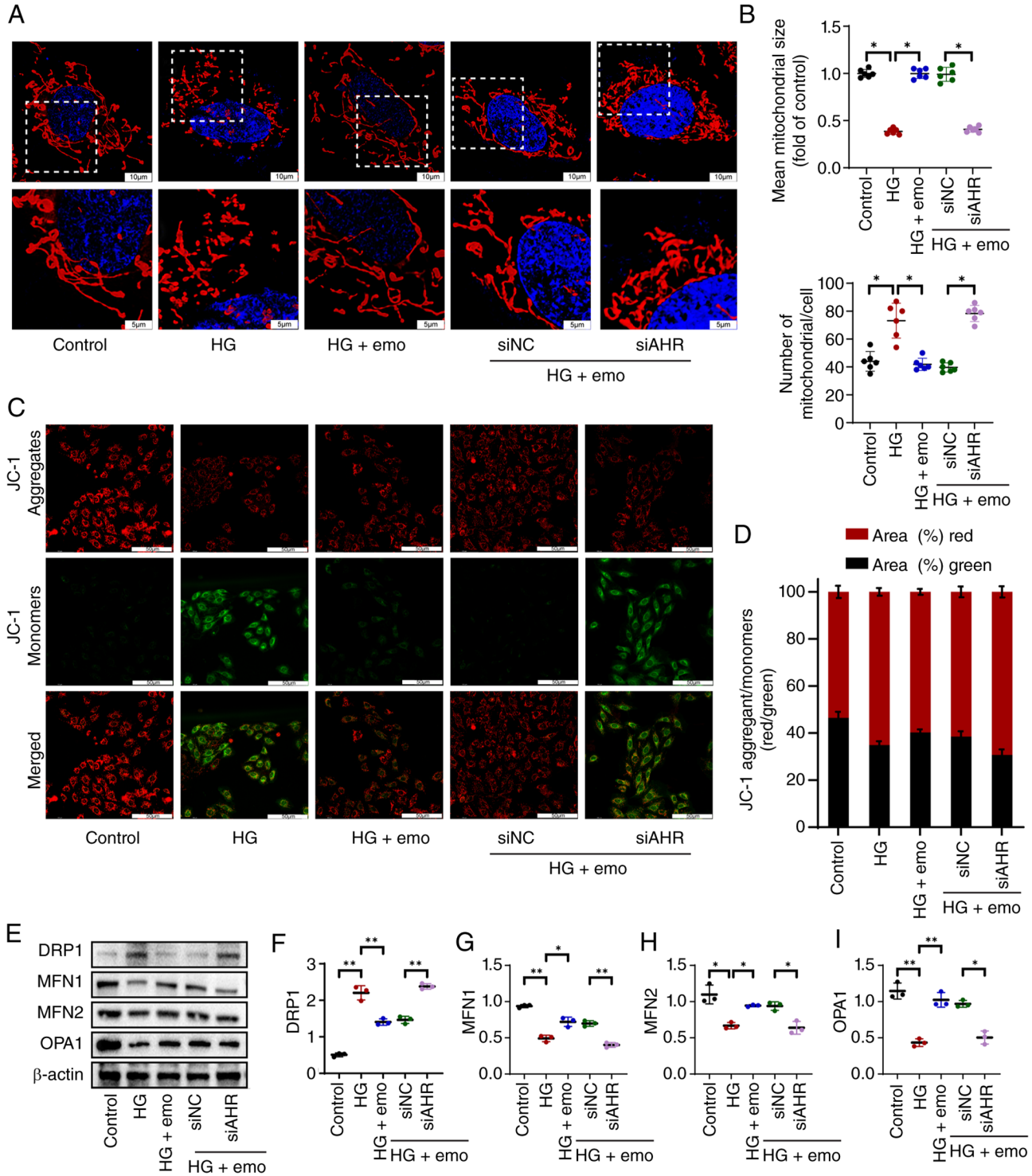


Figure 6. Emodin activates AHR to reshape the mitochondrial dynamic balance of cardiomyocytes induced by high glucose *in vitro*. (A) Morphological images of mitochondria in H9C2 cells under different intervention conditions. (B) Quantitative data on average mitochondrial size and the number of mitochondria per cell. (C and D) JC-1 staining to assess mitochondrial membrane potential in H9C2 cells. (E-I) Western blot analysis of the relative protein expression levels of DRP1, MFN1, MFN2 and OPA1 in cultured H9C2 cells. Data are presented as the mean ± SD (n=3). *P<0.05 and **P<0.01. AHR, aryl hydrocarbon receptor; DRP1, dynamin-related protein 1; MFN, mitochondrial fusion protein; OPA1, optic atrophy protein 1; HG, high-glucose; si-, small interfering; NC, negative control.

isolated parallel event but is intimately and sequentially coupled with the ferroptotic cascade. Therefore, Emodin-mediated AHR activation regulates mitochondrial dynamics, which is associated with the inhibition of ferroptosis.

Emo activates AHR to ease the imbalance mitochondrial dynamics in DCM mice. To verify whether emo alleviates DCM-induced mitochondrial dynamic imbalance in an AHR-dependent manner, cardiac-specific AHR knockdown was achieved via tail-vein injection of AAV9-shAhR. Successful viral transduction and efficient AHR silencing were confirmed by myocardial EGFP fluorescence and a significant reduction in AHR expression compared with the AAV9-shNC control (Fig. 7A and B; Fig. S3A). AHR silencing largely

abolished the cardioprotective effects of emo, as reflected by reduced LVEF and LVFS, increased LVIDd and LVIDs, and marked ventricular dilatation (Fig. 7C-G). Consistently, H&E, Masson and WGA staining showed aggravated myofiber disarray, interstitial fibrosis and cardiomyocyte hypertrophy in the AAV9-shAHR group compared with AAV9-sh-NC (Fig. 7H-L), indicating that AHR knockdown blunts Emo-mediated functional and structural benefits. Electron microscopy further revealed that AHR silencing negated the corrective effects of emo on mitochondrial dynamics, leading to severe ultrastructural damage (cristae disruption, matrix vacuolization, membrane rupture), reduced mean mitochondrial volume, and increased mitochondrial number per unit area (Fig. 7M). To quantify these ultrastructural pathologies, mitochondrial Flameng scoring was performed, which showed that the suppressive effect of emo on mitochondrial injury was attenuated following AHR knockdown (Fig. S3B). Furthermore, AHR silencing impaired the ability of emo to restore mitochondrial morphology, as evidenced by reduced mean mitochondrial volume and increased mitochondrial number per unit area (Fig. 7N and O). Given that mitochondrial dynamic disruption is associated with local ferroptotic cascades and iron pool dysregulation in the heart, tissue iron levels were also monitored and it was found that the regulatory effect of emo on limiting cardiac iron overload was suppressed in the AAV9-shAHR group, manifesting as a recurrence of myocardial iron accumulation (Fig. S3C). At the molecular level, western blotting confirmed a shift toward excessive mitochondrial fission, with DRP1 upregulation and MFN1, MFN2 and OPA1 downregulation (Fig. 7P-T). Collectively, these data demonstrate that emo exerts its anti-cardiac injury effects in DCM by engaging cardiac AHR transcriptional network to reshape mitochondrial dynamics and preserve myocardial iron homeostasis.

Discussion

In the present study, it was found that emo can inhibit cardiomyocyte apoptosis and myocardial fibrosis under high glucose stress, thereby effectively protecting cardiac ejection function in DCM. Further research revealed that emo can effectively restore mitochondrial respiratory chain enzyme activity and inhibit excessive mitochondrial fission, which is crucial for protecting cardiac function. Additionally, *in vitro* studies demonstrated that the aforementioned effects of emo require AHR mediation and are achieved by promoting Nrf2 nuclear translocation and activating the expression of downstream antioxidant molecules.

DCM is a condition affecting cardiac structure and function in patients with diabetes, independent of coronary heart disease, valvular heart disease and other cardiovascular diseases (26). It is characterized by metabolic disturbances, abnormalities in subcellular components and immunological changes, leading to local cardiac inflammation, oxidative stress, mitochondrial dysfunction and cell apoptosis. These changes cause impaired cardiac systolic and diastolic function, left ventricular hypertrophy and dilated cardiomyopathy, eventually leading to heart failure (2). Currently, the main treatments for DCM include controlling blood glucose, regulating blood lipids, improving microcirculation, and managing heart failure. However, these treatments primarily focus on managing the primary disease and alleviating complications, and there is a lack of effective specific therapies for DCM. Emo, as an antioxidant molecule, has been reported to have therapeutic effects in lung injury, cancer and diabetic nephropathy (10,27,28). Moreover, it has also been reported to significantly alleviate atherosclerosis in the cardiovascular system. The present study revealed that emo significantly alleviates cardiac damage caused by high blood glucose, primarily by inhibiting myocardial fibrosis, apoptosis and hypertrophy. By assessing oxidative stress-related markers such as SOD and MDA, it was found that the effects of emo are likely closely related to its antioxidant properties.

Mitochondria are essential organelles for energy production and maintaining normal cellular physiological functions, and their damage plays a significant role in the pathogenesis of DCM. In diabetic patients with impaired myocardial contraction, mitochondria often exhibit swelling and fragmentation, accompanied by impaired mitochondrial dynamics, suggesting that decreased myocardial contraction in diabetes may be related to deteriorated mitochondrial function (29). Damaged mitochondria, due to increased membrane permeability, release pro-apoptotic factors into the cytoplasm, contributing to cardiomyocyte apoptosis. Additionally, mitochondria are closely linked to oxidative stress. ROS are primarily produced through mitochondrial pathways, and there is a mutual promotion relationship between mitochondria and ROS (4,5). ROS are mainly generated by the electron transport chain located in the mitochondrial inner membrane, and excessive ROS can further damage mitochondrial DNA, proteins and membranes (6), exacerbating the dysfunction of the electron transport chain and leading to mitochondrial homeostasis disruption and ROS accumulation. Thus, excessive mitochondrial fission, due to its functional impairment, can be considered an upstream event of ROS production (30). Therefore, inhibiting pathological mitochondrial overfission and reducing cardiac oxidative stress are crucial for protecting cardiac function. The results of the present study indicated that emo significantly inhibits excessive mitochondrial fission and regulates the expression levels of mitochondrial dynamics proteins such as DRP1 and MFN2, shifting the mitochondrial dynamics towards fusion. Surprisingly, it was also found that emo significantly protects the enzyme activity of mitochondrial complexes, which is important for maintaining normal mitochondrial energy metabolism and reducing ROS production.

AHR, a member of the basic helix-loop-helix transcription factor family, regulates various systemic diseases, including skin inflammation and Parkinson's disease (11,13). It has been indicated that AHR can act as a transcription factor for Nrf2, modulating Nrf2 transcription (19). The AHR-Nrf2 pathway plays a crucial regulatory role in various inflammation and oxidative stress-related diseases (31,32). The present findings identified that AHR expression is impaired under high glucose stress, but emo can increase AHR levels in myocardial tissue. Importantly, molecular docking predictions revealed that emo has a strong binding affinity with AHR, indicating it as a potential ligand for AHR. Furthermore, fluorescence staining revealed that emo promotes the nuclear translocation of Nrf2 and increases the expression of downstream antioxidant molecules NQO1 and HO-1. Mechanistically, although AHR and Nrf2 are classically governed by

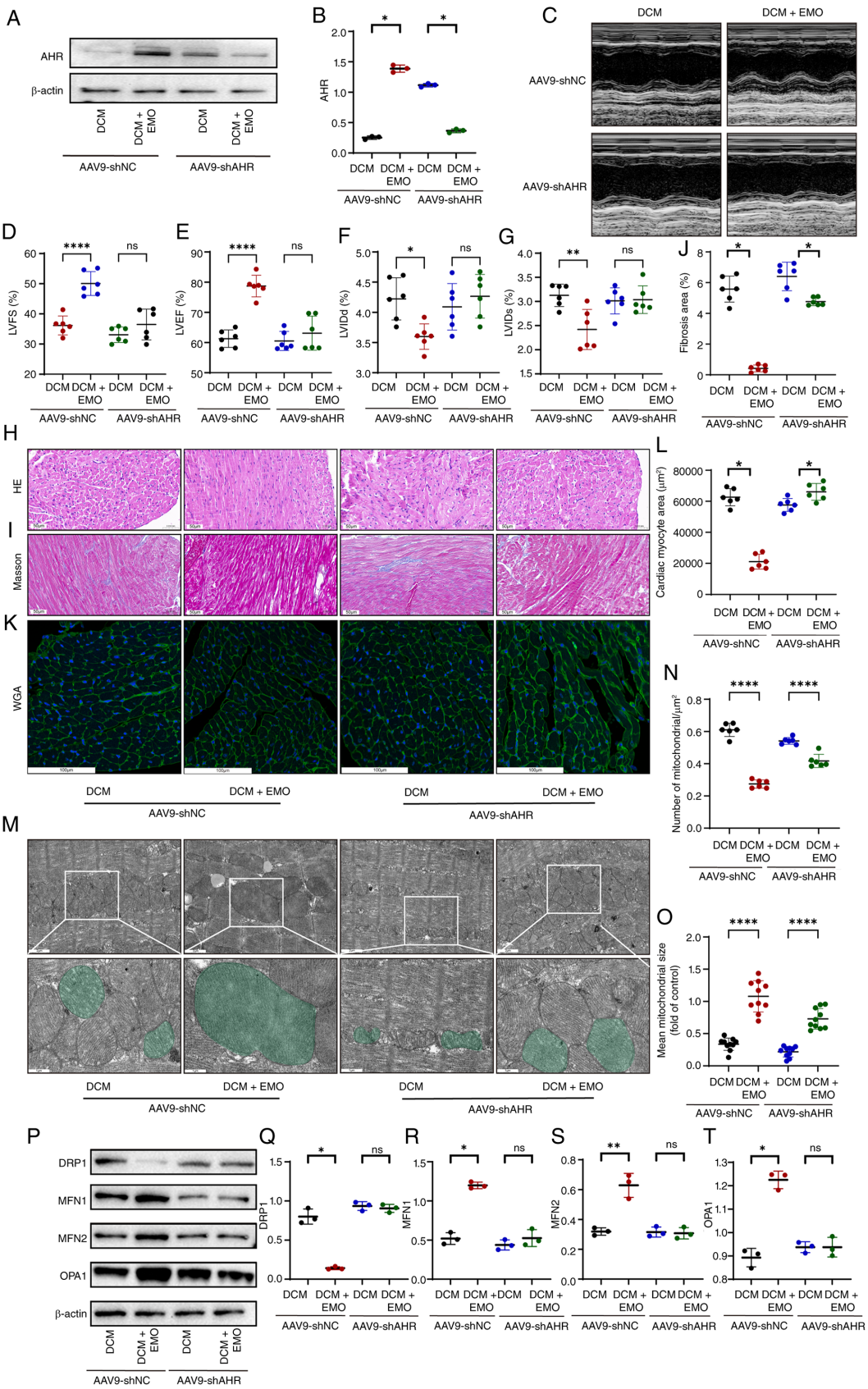


Figure 7. AHR knockdown attenuates the protective effects of emodin on cardiac function and mitochondrial dynamics in DCM mice. (A and B) AHR protein expression in heart tissues and validation of successful cardiac-specific knockdown by AAV9-cTnT-shAHR (labeled as AAV9-shAHR). (C-G) Assessment of cardiac function by echocardiography. (H-L) Histological evaluation of myocardial pathology and fibrosis. (M-O) Ultrastructural and quantitative analysis of mitochondria by transmission electron microscopy. (P-T) Protein levels of mitochondrial fission (DRP1) and fusion (MFN1, MFN2 and OPA1) regulators. Data are presented as the mean ± SD (n=6 independent animal experiments; n=3 independent western blot experiments). *P<0.05, **P<0.01 and ****P<0.0001. AHR, aryl hydrocarbon receptor; sh-, short hairpin; DRP1, dynamin-related protein 1; MFN, mitochondrial fusion protein; OPA1, optic atrophy protein 1; DCM, diabetic cardiomyopathy; NC, negative control; LVFS, left ventricular fractional shortening; LVID, left ventricular internal dimension; LVIDd, LVID at end-diastole; LVIDs, LVID at systole; ns, not statistically significant.

distinct pathways, AHR-ARNT binding to XRE elements and Keap1-mediated post-translational control of Nrf2, a non-canonical transcriptional link between them has been documented: Functional XRE-like elements within the Nrf2 promoter allow ligand-activated AHR to transactivate Nrf2 transcription, placing the Nrf2-ARE program downstream of AHR-XRE activation as a complement to the canonical Keap1 pathway (33). Consistent with this framework and with a recent study showing that the AHR ligand indole-3-lactic acid activates Nrf2 to inhibit ferroptosis in cardiomyocytes (34), the present findings indicated that Emodin drives Nrf2 activation in an AHR-dependent manner. Functionally, nuclear translocation of Nrf2, a definitive marker of its activation and a prerequisite for ARE binding and induction of target genes such as HO-1, NQO1 and GPX4, was robustly enhanced by Emodin. Although AHR-reporter and Nrf2-reporter assays were not performed, the coordinated nuclear enrichment of Nrf2, the upregulation of its downstream effectors, and the loss of these effects upon AHR silencing together provide strong functional evidence that Emodin engages an AHR-dependent Nrf2 antioxidant program. It is acknowledged that direct AHR occupancy on the Nrf2 promoter was not examined in the current cardiac model and represents a worthwhile direction for future mechanistic study. Subsequent siRNA-mediated AHR interference showed that the cardioprotective effects of emo significantly diminished. These lines of evidence collectively suggest that emo exerts its effects through the AHR-Nrf2 pathway. Furthermore, although direct pharmacokinetic translation between *in vitro* and *in vivo* models is complex, the selected *in vivo* dose of 30 mg/kg was proven highly effective in engaging this myocardial AHR pathway and reversing structural remodeling, aligning with the robust cytoprotection observed at 40 μM *in vitro*.

The limitations and strengths of the present study also warrant consideration. First, regarding the animal model, a combination of HFD feeding and low-dose STZ injection was utilized in wild-type C57BL/6J mice. The unique advantage of this non-genetic model is its ability to rapidly and stably induce severe glucolipid metabolic disorders alongside partial pancreatic β-cell decompensation, thereby effectively mimicking the core pathophysiological trajectory of advanced human type 2 DCM. This approach provides a highly reproducible platform for evaluating early pharmacological interventions. However, a notable limitation is that this accelerated chemical induction creates an exceptionally severe diabetic phenotype, which may not entirely capture the decades-long, gradual pathological evolution typical of human DCM. Furthermore, because of inherent genetic and cardiovascular differences between mice and humans, clinical studies are still required to validate these findings. Second, although the present study focused on oxidative stress, mitochondrial dynamics, ferroptosis and lipid peroxidation, numerous additional mechanisms underlying the onset and progression of DCM remain undefined. Future work will further dissect its pathogenesis and seek drug candidates with more precise, targeted regulatory effects.

In conclusion, it was first demonstrated that emo alleviates DCM-related myocardial injury by activating the AHR/Nrf2 pathway to concurrently inhibit ferroptosis and excessive mitophagy. Mechanistically, emo triggers the AHR-Nrf2 axis, thereby interrupting HG-induced mitochondrial over-fission and lipid peroxidation, which in turn suppresses cardiomyocyte ferroptosis and interstitial fibrosis. These effects substantially restore cardiac contractile performance in DCM mice and are completely abolished when AHR is silenced by siRNA, confirming pathway dependence. Emo represents a first-in-class, AHR-directed ferroptosis inhibitor ready for pre-clinical optimization and offers a promising therapeutic candidate for DCM and other ferroptosis-driven cardiomyopathies.

Acknowledgements

Not applicable.

Funding

The present study was supported by The Shaoxing Municipal Health Science and Technology Program Project (grant no. 2023SKY124), The Zhejiang Provincial Traditional Chinese Medicine Science and Technology Plan Project (grant no. 2025ZX043), The Zhejiang Provincial Medical and Health Science and Technology Program (grant no. 2025KY392) and the National Natural Science Foundation of China (grant no. 82200390).

Availability of data and materials

The data generated in the present study may be requested from the corresponding author.

Authors' contributions

XY managed data and wrote the original manuscript. HaL developed methodology, provided resources and conducted software analysis. JY managed data, conducted investigation, and wrote, reviewed and edited the manuscript. JZ conducted formal analysis, provided resources, and wrote and edited the manuscript. JZ and HaL developed methodology, provided resources, and wrote and edited the manuscript. JY and HuL managed data, conducted formal analysis, developed methodology, supervised the study, and wrote, reviewed and edited the manuscript. JC conceived and designed the study, acquired funding, and contributed to writing, reviewing, and editing the manuscript. JY and JC confirm the authenticity of all the raw data. All authors read and approved the final version of the manuscript.

Ethics approval and consent to participate

All animal protocols were approved by the Animal Care and Use Committee of Shaoxing People's Hospital (approval no. 2022C020; Shaoxing, China).

Patient consent for publication

Not applicable.

Competing interests

The authors declare that they have no competing interests.

References

1. Sun H, Saeedi P, Karuranga S, Pinkepank M, Ogurtsova K, Duncan BB, Stein C, Basit A, Chan JCN, Mbanya JC, *et al*: IDF diabetes atlas: Global, regional and country-level diabetes prevalence estimates for 2021 and projections for 2045. Diabetes Res Clin Pract 183: 109119, 2022.
2. Palomer X, Pizarro-Delgado J and Vázquez-Carrera M: Emerging actors in diabetic cardiomyopathy: Heartbreaker biomarkers or therapeutic targets? Trends Pharmacol Sci 39: 452-467, 2018.
3. Nakamura K, Miyoshi T, Yoshida M, Akagi S, Saito Y, Ejiri K, Matsuo N, Ichikawa K, Iwasaki K, Naito T, *et al*: Pathophysiology and treatment of diabetic cardiomyopathy and heart failure in patients with diabetes mellitus. Int J Mol Sci 23: 3587, 2022.
4. Sapian S, Taib IS, Latip J, Katas H, Chin KY, Mohd Nor NA, Jubaidi FF and Budin SB: Therapeutic approach of flavonoid in ameliorating diabetic cardiomyopathy by targeting mitochondrial-induced oxidative stress. Int J Mol Sci 22: 11616, 2021.
5. Tsutsui H, Kinugawa S and Matsushima S: Oxidative stress and heart failure. Am J Physiol Heart Circ Physiol 301: H2181-H2190, 2011.
6. Guo C, Sun L, Chen X and Zhang D: Oxidative stress, mitochondrial damage and neurodegenerative diseases. Neural Regen Res 8: 2003-2014, 2013.
7. Galaris D, Barbouti A and Pantopoulos K: Iron homeostasis and oxidative stress: An intimate relationship. Biochim Biophys Acta Mol Cell Res 1866: 118535, 2019.
8. Yang X, Kawasaki NK, Min J, Matsui T and Wang F: Ferroptosis in heart failure. J Mol Cell Cardiol 173: 141-153, 2022.
9. Zhang R, Chen J, Wang S, Zhang W, Zheng Q and Cai R: Ferroptosis in cancer progression. Cells 12: 1820, 2023.
10. Zhang Q, Chen WW, Sun X, Qian D, Tang DD, Zhang LL, Li MY, Wang LY, Wu CJ and Peng W: The versatile emodin: A natural easily acquired anthraquinone possesses promising anticancer properties against a variety of cancers. Int J Biol Sci 18: 3498-3527, 2022.
11. Semwal RB, Semwal DK, Combrinck S and Viljoen A: Emodin-A natural anthraquinone derivative with diverse pharmacological activities. Phytochemistry 190: 112854, 2021.
12. He Y, Xi J, Fang J, Zhang B and Cai W: Aloe-emodin alleviates doxorubicin-induced cardiotoxicity via inhibition of ferroptosis. Free Radic Biol Med 206: 13-21, 2023.
13. Hu S, Zhou J, Hao J, Zhong Z, Wu H, Zhang P, Yang J, Guo H and Chi J: Emodin ameliorates doxorubicin-induced cardiotoxicity by inhibiting ferroptosis through the remodeling of gut microbiota composition. Am J Physiol Cell Physiol 326: C161-C176, 2024.
14. Dai S, Ye B, Chen L, Hong G, Zhao G and Lu Z: Emodin alleviates LPS-induced myocardial injury through inhibition of NLRP3 inflammasome activation. Phytother Res 35: 5203-5213, 2021.
15. Zhang X, Qin Q, Dai H, Cai S, Zhou C and Guan J: Emodin protects H9c2 cells from hypoxia-induced injury by up-regulating miR-138 expression. Braz J Med Biol Res 52: e7994, 2019.
16. Wu Z, Chen Q, Ke D, Li G and Deng W: Emodin protects against diabetic cardiomyopathy by regulating the AKT/GSK-3β signaling pathway in the rat model. Molecules 19: 14782-14793, 2014.
17. Chaffin CL, Trewin AL and Hutz RJ: Estrous cycle-dependent changes in the expression of aromatic hydrocarbon receptor (AHR) and AHR-nuclear translocator (ARNT) mRNAs in the rat ovary and liver. Chem Biol Interact 124: 205-216, 2000.
18. Liu JR, Miao H, Deng DQ, Vaziri ND, Li P and Zhao YY: Gut microbiota-derived tryptophan metabolism mediates renal fibrosis by aryl hydrocarbon receptor signaling activation. Cell Mol Life Sci 78: 909-922, 2021.
19. Wang K, Lv Q, Miao YM, Qiao SM, Dai Y and Wei ZF: Cardamonin, a natural flavone, alleviates inflammatory bowel disease by the inhibition of NLRP3 inflammasome activation via an AhR/Nrf2/NQO1 pathway. Biochem Pharmacol 155: 494-509, 2018.
20. Chen J, Wang Q, Li R, Li Z, Jiang Q, Yan F and Ye J: The role of Keap1-Nrf2 signaling pathway during the progress and therapy of diabetic retinopathy. Life Sci 338: 122386, 2024.
21. He Z, Botchway BOA, Zhang Y and Liu X: Triptolide activates the Nrf2 signaling pathway and inhibits the NF-κB signaling pathway to improve Alzheimer disease. Metab Brain Dis 39: 173-182, 2024.
22. Bauer BM, Bhattacharya S, Bloom-Saldana E, Irimia-Dominguez JM and Fueger PT: Dose-dependent progression of multiple low-dose streptozotocin-induced diabetes in mice. Physiol Genomics 55: 381-391, 2023.
23. Parilla JH, Willard JR, Barrow BM and Zraika S: A mouse model of beta-cell dysfunction as seen in human type 2 diabetes. J Diabetes Res 2018: 6106051, 2018.
24. Livak KJ and Schmittgen TD: Analysis of relative gene expression data using real-time quantitative PCR and the 2(-Delta Delta C(T)) method. Methods 25: 402-408, 2001.
25. Cao Y, Chen Z, Hu J, Feng J, Zhu Z, Fan Y, Lin Q and Ding G: Mfn2 regulates high glucose-induced MAMs dysfunction and apoptosis in podocytes via PERK pathway. Front Cell Dev Biol 9: 769213, 2021.
26. Rawshani A, Rawshani A, Franzén S, Sattar N, Eliasson B, Svensson AM, Zethelius B, Miftaraj M, McGuire DK, Rosengren A and Gudbjörnsdottir S: Risk factors, mortality, and cardiovascular outcomes in patients with type 2 diabetes. N Engl J Med 379: 633-644, 2018.
27. Liu Y, Shang L, Zhou J, Pan G, Zhou F and Yang S: Emodin attenuates LPS-induced acute lung injury by inhibiting NLRP3 inflammasome-dependent pyroptosis signaling pathway in vitro and in vivo. Inflammation 45: 753-767, 2022.
28. Ji J, Tao P, Wang Q, Cui M, Cao M and Xu Y: Emodin attenuates diabetic kidney disease by inhibiting ferroptosis via upregulating Nrf2 expression. Aging (Albany NY) 15: 7673-7688, 2023.
29. Montaigne D, Marechal X, Coisne A, Debry N, Modine T, Fayad G, Potelle C, El Arid JM, Mouton S, Sebti Y, *et al*: Myocardial contractile dysfunction is associated with impaired mitochondrial function and dynamics in type 2 diabetic but not in obese patients. Circulation 130: 554-564, 2014.
30. Yu T, Robotham JL and Yoon Y: Increased production of reactive oxygen species in hyperglycemic conditions requires dynamic change of mitochondrial morphology. Proc Natl Acad Sci USA 103: 2653-2658, 2006.
31. Cui Q, Zhang Z, Tian X, Liang X, Lu Y, Shi Y, Kuerman M, Wang R, Zhou Y, Gong P, *et al*: Bifidobacterium bifidum ameliorates DSS-induced colitis in mice by regulating AHR/NRF2/NLRP3 inflammasome pathways through indole-3-lactic acid production. J Agric Food Chem 71: 1970-1981, 2023.
32. Li H, Yuan Y, Chen H, Dai H and Li J: Indoleamine 2,3-dioxygenase mediates the therapeutic effects of adipose-derived stromal/stem cells in experimental periodontitis by modulating macrophages through the kynurenine-AhR-NRF2 pathway. Mol Metab 66: 101617, 2022.
33. Miao W, Hu L, Scrivens PJ and Batist G: Transcriptional regulation of NF-E2 p45-related factor (NRF2) expression by the aryl hydrocarbon receptor-xenobiotic response element signaling pathway: Direct cross-talk between phase I and II drug-metabolizing enzymes. J Biol Chem 280: 20340-20348, 2005.
34. Lian J, Lin H, Zhong Z, Song Y, Shao X, Zhou J, Xu L, Sun Z, Yang Y, Chi J, *et al*: Indole-3-lactic acid inhibits doxorubicin-induced ferroptosis through activating Aryl hydrocarbon receptor/Nrf2 signalling pathway. J Cell Mol Med 29: e70358, 2025.

Copyright © 2026 Yu et al. This work is licensed under a Creative Commons Attribution-NonCommercial-NoDerivatives 4.0 International (CC BY-NC-ND 4.0) License.